Controlling photoelectron interference along the quantization axis of multiphoton ionization in circularly polarized fields

Yankun Dou,[1] Xiaoxiao Long,[1] Peizeng Li,[1] Peipei Ge,[1] Yongkai Deng,[1] Qihuang Gong,[1,2,3] and Yunquan Liu[1,2,3]

[1]*State Key Laboratory for Mesoscopic Physics and Frontiers Science Center for Nano-Optoelectronics, School of Physics, Peking University, Beijing 100871, China*

[2]*Beijing Academy of Quantum Information Sciences, Beijing 100193, China*

[3]*Collaborative Innovation Center of Extreme Optics, Shanxi University, Taiyuan, Shanxi 030006, China*

(Received 24 October 2023; revised 16 May 2024; accepted 16 July 2024; published 2 August 2024)

We measure angle- and phase-resolved photoelectron momentum distributions of multiphoton ionization of xenon atoms using bicircular laser fields. In our experiment, the continuum electron ring currents with larger orbital angular momentum are prepared by an intense circular polarized laser field at 400 nm and probed with a spatiotemporally overlapped corotating or counter-rotating weak 800 nm laser pulse. Interestingly, a distinct "carpetlike" interference pattern in the direction of laser propagation is observed for the counter-rotating fields, but not for the corotating fields. By analyzing the momentum-resolved photoelectron yield oscillations with respect to the two-color relative phase (phase-of-the-phase spectrum), we observe a distinct angular dependence in the phase-of-the-phase spectrum in the laser propagation plane when the fields are counter-rotating. In contrast, in the corotating geometry, the phase-of-the-phase spectrum in the laser propagation plane displays an isotropic phase profile. We explain that the carpetlike interference in the propagation plane arises from the constructive and destructive interference of the continuum electron ring currents with different magnetic quantum number, which can be controlled by the light helicity.

DOI: 10.1103/PhysRevA.110.023101

I. INTRODUCTION

In the quantum world, the angular momentum of electrons is quantized. The electrons circle around the nucleus and carry an orbital angular momentum. The orbital angular momentum can be projected on the quantization axis, giving rise to quantized magnetic angular momentum $m\hbar$ (m is the magnetic quantum number). Within this physical picture, electrons with a certain orbital angular momentum can be regarded as ring-current electronic states [1]. Generally, ring currents carry an angular phase factor $e^{im\varphi}$ (φ is the azimuth angle), directly corresponding to the angular phase $m\varphi$ of the electrons. The sign and magnitude of m determine the direction and angular speed of rotation, respectively. Ring currents with the same angular speed but with different helicities, i.e., m and $-m$ can be viewed as a pair of enantiomers. Thus photoionization of ring currents via multiphoton absorption or tunneling by chiral light fields has garnered significant attention [2–6]. Recent theoretical [7–10] and experimental [11,12] studies illustrate that circularly polarized light fields preferentially ionize counter-rotating ground-state electron ring currents relative to the light fields. This feature allows for the production of spin-polarized photoelectrons [13–16] and control of electron-spin dynamics [17–19] in the strong-field regime.

The interaction between electron ring currents and circularly polarized laser pulses has attracted much attention due to the natural chiral phase structure of electron ring currents [17–27]. For instance, an unusual type of Ramsey interference between time-delayed electron ring currents with different magnetic quantum numbers m, produced by a pair of counter-rotating circularly polarized pulses, was investigated theoretically [20,21] and later confirmed experimentally [22,23]. Moreover, circular dichroism of excited ring currents during photoionization [24] and spin-orbit time delay of the electron ring currents have been investigated [25]. With advancements in attosecond technology, attosecond chiral dynamics of electron ring currents have been manipulated and probed using the attosecond circular-dichroism chronoscopy [26].

In the strong-field regime, previous studies have focused on photoelectron momentum distribution (PMD) in the laser polarization plane, revealing novel interference structures, such as the interference carpet, spiral structures, and spider structures [28–30]. Recent studies on the photoionization of the ring currents with circularly polarized fields have also focused on the PMD in the laser polarization plane [24,25]. In contrast, the PMD in the laser propagation plane has received much less attention, despite containing valuable information, such as the nondipole effect in strong-field ionization and chiral dynamics of photoionization by chiral laser fields [31–34]. Recently, subcycle interference has been experimentally observed in the photoelectron momentum spectrum along the light propagation direction in the ionization of helium by two-color circularly polarized laser fields [35].

In this work, we investigate the photoelectron circular dichroism of continuum electron ring currents with high orbital angular momentum in the light propagation plane using sculptured circular fields. Continuum electron ring currents with well-defined helicity are prepared by multiphoton ionization of xenon atoms with an intense circularly polarized

laser field at 400 nm. We then probe the circular dichroism of electron ring currents with a weak, synchronized corotating or counter-rotating 800 nm laser pulse. We observe that the PMD in the light propagation plane for the counter-rotating geometry reveals a remarkable carpetlike interference structure compared to the corotating case. Additionally, by extracting the phase-of-the-phase (POP) spectra of PMDs in the laser propagation plane, we find that the phase structure in the counter-rotating case exhibits prominent angular dependences. Notably, the phase structure shows a distinct π shift between emissions along the laser propagation direction and in the polarization plane when the fields are counter-rotating. In contrast, in the corotating geometry, the angular-resolved phase structure is nearly isotropic. Our findings are supported by solving the time-dependent Schrödinger equation (TDSE). Insights gained from the calculations allow us to determine a complete set of amplitudes and phases of the contributed partial-wave states and explain the carpetlike interference.

II. EXPERIMENTAL SCHEME AND RESULTS

Experimentally, 800 nm fundamental laser pulses with a 25 fs duration and 3 kHz repetition frequency were produced from a commercial amplified Ti:sapphire femtosecond laser system. We obtained second-harmonic pulses at 400 nm by frequency doubling through a 200-μm-thick β-barium borate crystal. The second-harmonic field with circular polarization was used as the ionizing light field. The peak intensity of the 400 nm circularly polarized light field was calibrated to be $\sim 6.3 \times 10^{13}\,\mathrm{W/cm^2}$, according to the positions of above-threshold ionization (ATI) peaks in the photoelectron energy spectrum [36–38]. Here, the laser intensity of the 800 nm circular pulse is estimated to be $\sim 4.5 \times 10^{12}\,\mathrm{W/cm^2}$ by comparing the measured PMDs with the solution of the TDSE. We use a pair of fused silica wedges to finely adjust the relative phase φ between the two-color laser pulses. The laser pulses were then focused onto a thin supersonic beam of xenon atoms inside of a cold-target recoil-ion momentum spectroscopy (COLTRIMS) [39,40]. The three-dimensional momenta of electrons were measured by a time-of-flight spectrometer equipped with a position-sensitive detector, in which a homogeneous static electric field (∼3.2 V/cm) and magnetic field (∼5.5 G) were used to collect an electron and an ion in coincidence for each event [41–43].

Figure 1 illustrates the experimental scheme. An intense 400 nm circular field is employed to trigger the multiphoton ionization of xenon atoms. The light propagates along the y axis, with its polarization in the x-z plane. Consequently, the y axis serves as the quantization axis for the interaction of atoms with circularly polarized fields. The measured PMDs in the x-z and y-z planes with high resolution are also shown, respectively. The ATIs are clearly visible in both the laser polarization plane and the laser propagation plane. In the light polarization plane, the PMDs are isotropic, revealing concentric ring structures due to the circular polarization of the light fields.

Different from previous studies [44,45], our work focuses on the PMD in the light propagation plane, i.e., the y-z plane. When using circularly polarized fields, almost no ionization events occur along the quantization axis. The momentum distribution along the p_x direction in circularly polarized laser fields is nearly Gaussian. Recently, Arissian *et al.* have measured the width of the PMD along the laser propagation direction in a circularly polarized laser field for Ne and Ar atoms [46]. Thereafter, the nonadiabatic effect on the momentum distribution along the propagation direction has been intensively studied [42,47].

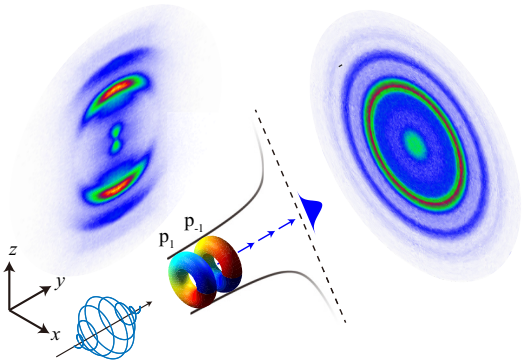

FIG. 1. Experimental scheme. We used an intense circular field at 400 nm to ionize the xenon atoms. The quantization axis is along the y axis. The measured PMDs in the laser polarization plane (x, z) and propagation plane (y, z) are shown as the side view, which are slices along $p_y = 0$ and $p_x = 0$ in three-dimensional (3D) PMD, respectively.

We then add weak, spatiotemporally overlapped 800 nm corotating or counter-rotating circularly polarized laser fields to probe the continuum electron ring currents prepared by multiphoton ionization at 400 nm. Since the net angular momentum direction of the ring currents and the spin angular momentum direction of the light fields are both along the y axis, the circular dichroism would also manifest in the light propagation direction. Figures 2(a) and 2(b) show the two-color phase-integrated PMDs in the laser propagation plane for co- and counter-rotating geometries. One can observe that, after adding a weak 800 nm circular field, the PMDs are significantly modified.

Interestingly, different from the case in corotating fields as shown in Fig. 2(a), interference structures form in the laser propagation plane for the counter-rotating circular fields, as indicated by the rectangle outlined by the red dashed line in Fig. 2(b). This interference pattern resembles the carpetlike structure observed in the laser polarization plane with linear polarization [28], which was caused by the interference between electron wave packets ionized at the two peaks of the laser field per cycle, resulting in a 2ω separation of the ATI rings. Recently, it was shown that the spiral-like trajectory caused by forward rescattering is responsible for the carpetlike structure in the laser polarization plane [29].

Varying the two-color relative phase modulates the PMDs. Here, we employ phase-of-the-phase spectroscopy to analyze the phase-dependent PMD [48]. For each final momentum (p_y, p_z), the photoelectron yield $Y(\varphi)$ in the y-z plane changes as a function of the relative phase, i.e., $Y(\varphi) = Y_0 + \Delta Y \cos(\varphi + \Phi)$, where Y_0 is the background count, ΔY is the relative phase contrast (RPC), and Φ is the phase of the

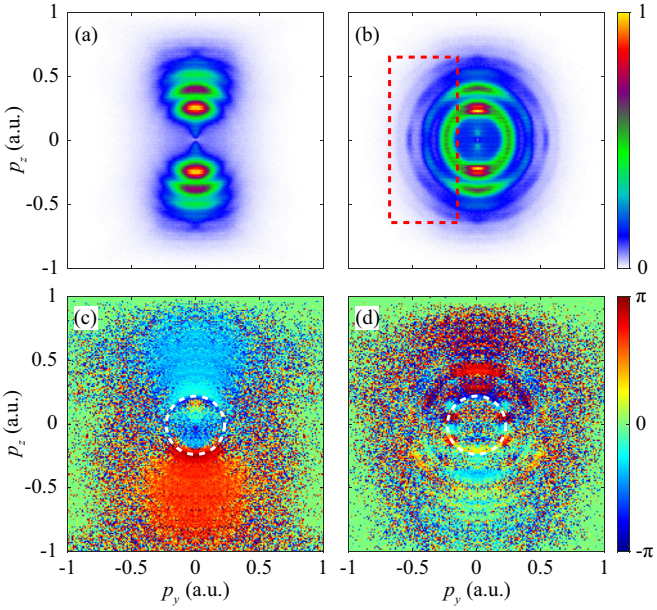

FIG. 2. (a),(b) The measured 2D PMDs in the laser propagation plane (slices at $p_y = 0$) for the corotating and counter-rotating circular fields, respectively. One can observe the interference structure in the red square in (b). (c),(d) The POP spectra for the PMDs for the corotating and counter-rotating circular fields, respectively.

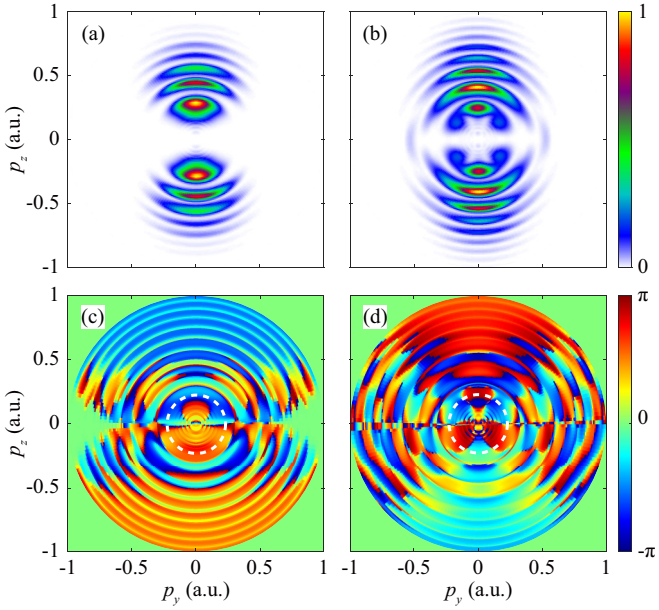

FIG. 3. (a),(b) The calculated 2D PMDs in the laser propagation plane (slices at $p_y = 0$) for the corotating and counter-rotating circular fields with TDSE, respectively. (c),(d) The momentum-resolved POP spectra with the TDSE for the corotating and counter-rotating circular fields, respectively.

phase (POP). Mathematically, the RPC and POP spectra can be extracted via fast Fourier transform of $Y(\varphi)$ with respect to φ for each (p_y, p_z). The extracted momentum-resolved POP spectra are shown in Figs. 2(c) and 2(d) for the corotating and counter-rotating cases, respectively. The results for the two interaction geometries exhibit very different features. In the corotating case, the POP hardly changes with respect to the emission angle $\theta = \arccos(p_y/p_{\text{total}})$ for electrons with $p_z > 0$ or $p_z < 0$. However, for the counter-rotating case, the POP changes significantly with the emission angle θ. Particularly, there is an abrupt phase jump between the emissions along the laser propagation direction and in the polarization plane.

III. THEORETICAL SIMULATIONS AND DISCUSSIONS

To understand the observation, we resort to the solution of the TDSE. In the TDSE simulation, we adopt an effective potential $V_{\text{eff}} = -[Z + (Z_{\text{full}} - Z)\exp(-r/r_s)]/r$ to model the $5p$ ground state of the xenon atom. Here, $Z = 1$ and $Z_{\text{full}} = 54$ are the asymptotic ion charges as $r \to \infty$ and $r \to 0$, respectively. The screening length $r_s = 0.102826$ is tuned to match the ionization potential ($I_p = 0.4458$ a.u.) of the $P_{3/2}$ ionic state for xenon atoms. The laser field has a 12-cycle pulse duration at 400 nm and a 6-cycle 800 nm pulse with a $\sin^2$ envelope. We separately calculate the ionization of $5p$ orbitals with the magnetic quantum number m at ± 1, 0. Then, we sum up the photoelectron momentum distributions of the three channels to obtain the final PMD. Twenty two-color relative phases within $[0, 2\pi]$ are sampled during the simulation to obtain the phase-integrated and phase-resolved PMDs.

Figures 3(a) and 3(b) show the simulated two-color phase-integrated PMDs in the laser propagation plane by solving TDSE for the corotating and counter-rotating circular fields, respectively. The TDSE calculations reproduce the measured PMDs well, including the carpetlike interference structure that emerges in the counter-rotating case. Based on the calculated phase-resolved TDSE calculations, we also extract the POP spectra in the laser propagation plane for these two field geometries, as shown in Figs. 3(c) and 3(d). Clearly, the simulations basically reproduce the experimental measurement as shown in Figs. 2(c) and 2(d).

To visualize the angle-dependent feature of POP in co- and counter-rotating fields, we show the angle-resolved POP spectra for the first-order sideband (as denoted by the white dashed lines in Figs. 2 and 3) in Figs. 4(a) and 4(b). One can clearly see that, for the corotating case, the angular-resolved POP spectrum is flat, with the phase around $-\pi/2$ at different emission angles. However, for the counter-rotating case, there is an abrupt phase jump ranging from $\sim -\pi/2$ to $\pi/2$ when the emission changes from the direction of the y axis to the laser polarization plane.

As the angular-dependent features are usually associated with the angular momentum of electrons, we illustrate the involved multiphoton transitions and the electron partial waves for the first-order ATI, second-order ATI, and sideband in corotating and counter-rotating geometries in Figs. 4(c) and 4(d), respectively. By absorbing the circular photons at 400 nm, the continuum ring-current states with high orbital angular momentum are generated. Given the ionization potential of xenon atoms, at least five photons of 400 nm are required to ionize the ground-state electrons of the xenon atoms. According to the selection rule of both l and m, when

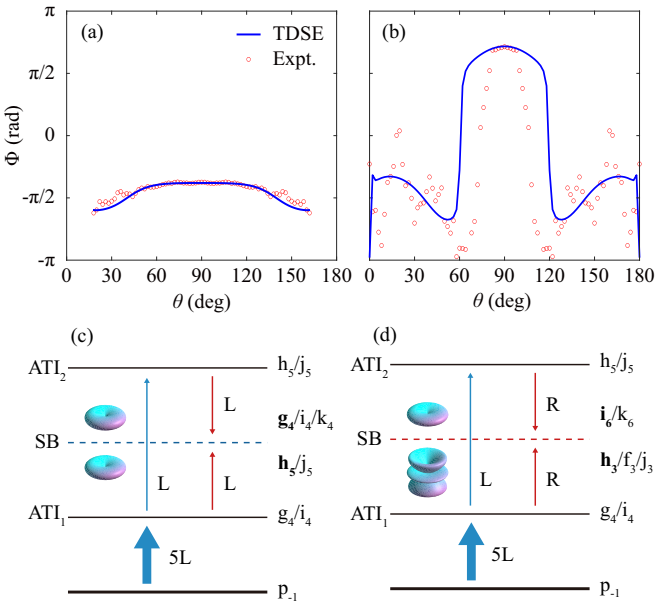

FIG. 4. (a),(b) Extracted angle-resolved POP spectra for the first-order sideband in the corotating and counter-rotating geometries. (c),(d) Multiphoton transition pathways for the corotating and counter-rotating geometries, Where L/R stands for the left/right circular polarization. The main contributed states for the first-order ATI, first-order sideband, and second-order ATI are shown on the right sides of (c),(d).

the electron absorbs a left- (right-) handed circular photon, its orbital angular momentum l changes by ± 1, and the magnetic quantum number m increases (decreases) by 1. As a result, the first-order ATI electrons can be regarded as mixed ring currents consisting of a partial wave of g4 ($l = 4$, $m = 4$) and $i4(l = 6, m = 4)$, while the second-order ATI electrons are mixed ring currents composed of $h5$ ($l = 5$, $m = 5$) and $j5(l = 7, m = 5)$.

The first-order sideband is formed by the interference between the two transition pathways, i.e., absorption of one 800 nm photon from the first-order ATI and emission of one 800 nm photon from the second-order ATI. In this case, the partial-wave components in the first-order sideband are illustrated in Figs. 4(c) and 4(d). In corotating fields, the first-order sideband comprises $h5$, $j5$, $g4$, $i4$, and $k4$ partial waves. In the counter-rotating case, the sideband is formed by interference between mixed $h3$, $f3$, $j3$, $i6$, and $k6$ partial waves. The involved partial waves determine the angular dependences of the PMDs and the POP spectra in co and counter-rotating fields.

Furthermore, to better understand the carpetlike interference structure and angular-dependent POP spectra, we identify the amplitude and phase of each contributed partial wave based on the TDSE method. Theoretically, we have transformed momentum spectra via Fourier transform and obtained the individual partial wave by expanding the final wave function into spherical harmonics [49,50]. Figures 5(a) and 5(b) show the extracted amplitudes and phases of the contributed partial waves for the first-order sideband in the corotating and counter-rotating geometries, respectively.

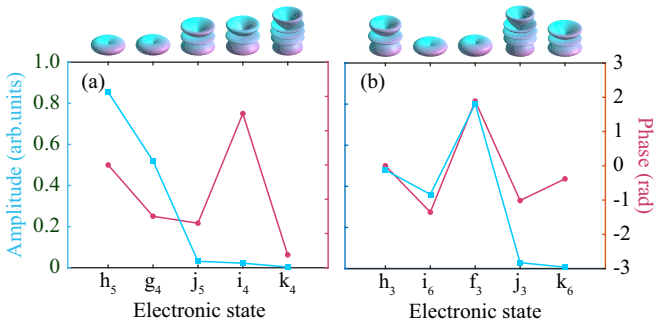

FIG. 5. Extracted amplitude and phase of the relevant partial waves for the first-order sideband in the corotating (a) and counter-rotating (b) geometries.

The amplitude and phase of the contributed partial wave differ significantly for the two interaction geometries. The helicity of the probing light of 800 nm can significantly modulate the involved partial waves.

In the corotating case, as seen in Fig. 5(a), the $h5$ ($l = 5$, $m = 5$) and $g4$ ($l = 4$, $m = 4$) waves dominate over the $j5$ ($l = 7$, $m = 5$), $i4$ ($l = 6$, $m = 4$), and $k4$ ($l = 8$, $m = 4$) waves. However, in the counter-rotating case, the $h3$ ($l = 5$, $m = 3$), $i6$ ($l = 6$, $m = 6$), and $f3$ ($l = 3$, $m = 3$) waves dominate over the $j3$ ($l = 7$, $m = 3$) and $k6$ ($l = 8$, $m = 6$) waves. Besides the amplitude of the contributed partial waves, their phases also provide a unique view of the photoionization dynamics of continuum electron ring currents. In the two geometries, the different angle-dependent phase changes in the POP spectra are mainly due to interference among the different partial waves. In the corotating case, the sideband is dominated by interference between the $h5$ and $g4$ waves, forming an almost isotropic phase profile, as seen in Fig. 4(a). In contrast, in the counter-rotating case, the angular-resolved POP spectrum for the first-order sideband undergoes a distinct phase shift of π, mainly due to the interference among the $h3$, $i6$, and $f3$ waves. Unlike the corotating case, the presence of the $h3$ partial wave in counter-rotating fields significantly influences the interference of electron ring currents due to its angular structure in the light propagation plane, thus leading to carpetlike interference. Moreover, its angular-dependent phase structure, i.e., the alternating phase sign of the three lobes in the $h3$ partial wave, also influences the interference among the $h3$, $i6$, and $f3$ waves, causing the phase jump in the angular-dependent POP spectrum.

IV. CONCLUSION

In conclusion, we have studied the photoelectron circular dichroism of electron ring currents using bicircular laser fields. The carpetlike interference in the light propagation plane was observed in the counter-rotating geometry. By extracting the phase-of-the-phase spectra, we show that the angular-dependent POP spectra exhibit prominent circular dichroism. Insights gained from the TDSE simulation enable us to determine a complete set of partial waves contributing to the continuum electron ring currents. We revealed that the

circular dichroism related to the ring current can be probed and controlled with light helicity. The photoelectron interference structure along the laser propagation direction, obtained with counter-rotating fields, may find applications in chiral molecules [51,52], topological condensed matter [53], and the nondipole effect [54].

ACKNOWLEDGMENTS

This work is supported by the National Key Research and Development Program of China (Grant No. 2022YFA1604301) and the National Science Foundation of China (Grants No. 12334013, No. 92050201, and No. 92250306).

[1] I. Barth and J. Manz, Phys. Rev. A **75**, 012510 (2007).
[2] J. Hofbrucker, A. V. Volotka, and S. Fritzsche, Phys. Rev. Lett. **121**, 053401 (2018).
[3] N. Böwering, T. Lischke, B. Schmidtke, N. Müller, T. Khalil, and U. Heinzmann, Phys. Rev. Lett. **86**, 1187 (2001).
[4] I. Barth and O. Smirnova, J. Phys. B **47**, 204020 (2014).
[5] M. Han, P. Ge, Y. Fang, and Y. Liu, Phys. Rev. A **107**, 063104 (2023).
[6] J. H. Bauer, F. Mota-Furtado, P. F. O'Mahony, B. Piraux, and K. Warda, Phys. Rev. A **90**, 063402 (2014).
[7] I. Barth and O. Smirnova, Phys. Rev. A **84**, 063415 (2011).
[8] I. Barth and O. Smirnova, Phys. Rev. A **87**, 013433 (2013).
[9] I. Barth and O. Smirnova, Phys. Rev. A **87**, 065401 (2013).
[10] M.-M. Liu, M. Li, Y. Shao, M. Han, Q. Gong, and Y. Liu, Phys. Rev. A **96**, 043410 (2017).
[11] T. Herath, L. Yan, S. K. Lee, and W. Li, Phys. Rev. Lett. **109**, 043004 (2012).
[12] S. Eckart, M. Kunitski, M. Richter, A. Hartung, J. Rist, F. Trinter, K. Fehre, N. Schlott, K. Henrichs, L. P. H. Schmidt, T. Jahnke, M. Schöffler, K. Liu, I. Barth, J. Kaushal, F. Morales, M. Ivanov, O. Smirnova, and R. Dörner, Nat. Phys. **14**, 701 (2018).
[13] I. Barth and O. Smirnova, Phys. Rev. A **88**, 013401 (2013).
[14] A. Hartung, F. Morales, M. Kunitski, K. Henrichs, A. Laucke, M. Richter, T. Jahnke, A. Kalinin, M. Schöffler, L. Ph. H. Schmidt, M. Ivanov, O. Smirnova, and R. Dörner, Nat. Photonics **10**, 526 (2016).
[15] M.-M. Liu, Y. Shao, M. Han, P. Ge, Y. Deng, C. Wu, Q. Gong, and Y. Liu, Phys. Rev. Lett. **120**, 043201 (2018).
[16] D. Trabert, A. Hartung, S. Eckart, F. Trinter, A. Kalinin, M. Schöffler, L. Ph. H. Schmidt, T. Jahnke, M. Kunitski, and R. Dörner, Phys. Rev. Lett. **120**, 043202 (2018).
[17] D. B. Milošević, Phys. Rev. A **93**, 051402(R) (2016).
[18] D. Ayuso, A. Jiménez-Galán, F. Morales, M. Ivanov, and O. Smirnova, New J. Phys. **19**, 073007 (2017).
[19] M. Han, P. Ge, M.-M. Liu, Q. Gong, and Y. Liu, Phys. Rev. A **99**, 023404 (2019).
[20] J. M. Ngoko Djiokap, S. X. Hu, L. B. Madsen, N. L. Manakov, A. V. Meremianin, and A. F. Starace, Phys. Rev. Lett. **115**, 113004 (2015).
[21] J. M. Ngoko Djiokap, A. V. Meremianin, N. L. Manakov, S. X. Hu, L. B. Madsen, and A. F. Starace, Phys. Rev. A **94**, 013408 (2016).
[22] D. Pengel, S. Kerbstadt, L. Englert, T. Bayer, and M. Wollenhaupt, Phys. Rev. A **96**, 043426 (2017).
[23] D. Pengel, S. Kerbstadt, D. Johannmeyer, L. Englert, T. Bayer, and M. Wollenhaupt, Phys. Rev. Lett. **118**, 053003 (2017).
[24] M. Han, P. Ge, Y. Fang, X. Yu, Z. Guo, Y. Deng, Q. Gong, and Y. Liu, Phys. Rev. A **101**, 043406 (2020).
[25] P. Ge, Y. Fang, Z. Guo, X. Ma, X. Yu, M. Han, C. Wu, Q. Gong, and Y. Liu, Phys. Rev. Lett. **126**, 223001 (2021).
[26] M. Han, J.-B. Ji, T. Balčiūnas, K. Ueda, and H. J. Wörner, Nat. Phys. **19**, 230 (2023).
[27] M. Han, P. Ge, Y. Shao, Q. Gong, and Y. Liu, Phys. Rev. Lett. **120**, 073202 (2018).
[28] Ph. A. Korneev, S. V. Popruzhenko, S. P. Goreslavski, T.-M. Yan, D. Bauer, W. Becker, M. Kübel, M. F. Kling, C. Rödel, M. Wünsche, and G. G. Paulus, Phys. Rev. Lett. **108**, 223601 (2012).
[29] A. S. Maxwell, Carla Figueira de Morisson Faria, Y. Lai, R. Sun, and X.-J. Liu, Phys. Rev. A **102**, 033111 (2020).
[30] D. D. Hickstein, P. Ranitovic, S. Witte, X.-M. Tong, Y. Huismans, P. Arpin, X. Zhou, K. E. Keister, C. W. Hogle, B. Zhang, C. Ding, P. Johnsson, N. Toshima, M. J. J. Vrakking, M. M. Murnane, and H. C. Kapteyn, Phys. Rev. Lett. **109**, 073004 (2012).
[31] C. T. L. Smeenk, L. Arissian, B. Zhou, A. Mysyrowicz, D. M. Villeneuve, A. Staudte, and P. B. Corkum, Phys. Rev. Lett. **106**, 193002 (2011).
[32] A. Hartung, S. Eckart, S. Brennecke, J. Rist, D. Trabert, K. Fehre, M. Richter, H. Sann, S. Zeller, K. Henrichs, G. Kastirke, J. Hoehl, A. Kalinin, M. S. Schöffler, T. Jahnke, L. P. H. Schmidt, M. Lein, M. Kunitski, and R. Dörner, Nat. Phys. **15**, 1222 (2019).
[33] A. Hartung, S. Brennecke, K. Lin, D. Trabert, K. Fehre, J. Rist, M. S. Schöffler, T. Jahnke, L. Ph. H. Schmidt, M. Kunitski, M. Lein, R. Dörner, and S. Eckart, Phys. Rev. Lett. **126**, 053202 (2021).
[34] E. Bloch, S. Larroque, S. Rozen, S. Beaulieu, A. Comby, S. Beauvarlet, D. Descamps, B. Fabre, S. Petit, R. Taïeb, A. J. Uzan, V. Blanchet, N. Dudovich, B. Pons, and Y. Mairesse, Phys. Rev. X **11**, 041056 (2021).
[35] S. Eckart, M. Kunitski, I. Ivanov, M. Richter, K. Fehre, A. Hartung, J. Rist, K. Henrichs, D. Trabert, N. Schlott, L. Ph. H. Schmidt, T. Jahnke, M. S. Schöffler, A. Kheifets, and R. Dörner, Phys. Rev. A **97**, 041402(R) (2018).
[36] P. Agostini, F. Fabre, G. Mainfray, G. Petite, and N. K. Rahman, Phys. Rev. Lett. **42**, 1127 (1979).
[37] M. Li, M.-M. Liu, J.-W. Geng, M. Han, X. Sun, Y. Shao, Y. Deng, C. Wu, L.-Y. Peng, Q. Gong, and Y. Liu, Phys. Rev. A **95**, 053425 (2017).
[38] M. Han, P. Ge, Y. Shao, M.-M. Liu, Y. Deng, C. Wu, Q. Gong, and Y. Liu, Phys. Rev. Lett. **119**, 073201 (2017).
[39] R. Dörner, V. Mergel, O. Jagutzki, L. Spielberger, J. Ullrich, R. Moshammer, and H. Schmidt-Böcking, Phys. Rep. **330**, 95 (2000).

[40] J. Ullrich, R. Moshammer, A. Dorn, R. Dörner, L. Ph. H. Schmidt, and H. Schmidt-Böcking, Rep. Prog. Phys. **66**, 1463 (2003).
[41] M. Li, J.-W. Geng, H. Liu, Y. Deng, C. Wu, L.-Y. Peng, Q. Gong, and Y. Liu, Phys. Rev. Lett. **112**, 113002 (2014).
[42] M. Li, J.-W. Geng, M. Han, M. M. Liu, L.-Y. Peng, Q. Gong, and Y. Liu, Phys. Rev. A **93**, 013402 (2016).
[43] M. M. Liu, M. Li, C. Wu, Q. Gong, A. Staudte, and Y. Liu, Phys. Rev. Lett. **116**, 163004 (2016).
[44] Y. Huismans *et al.*, Science **331**, 61 (2011).
[45] D. M. Villeneuve, P. Hockett, M. J. J. Vrakking, and H. Niikura, Science **356**, 1150 (2017).
[46] L. Arissian, C. Smeenk, F. Turner, C. Trallero, A. V. Sokolov, D. M. Villeneuve, A. Staudte, and P. B. Corkum, Phys. Rev. Lett. **105**, 133002 (2010).
[47] I. Dreissigacker and M. Lein, Chem. Phys. **414**, 69 (2013).
[48] S. Skruszewicz, J. Tiggesbäumker, K.-H. Meiwes-Broer, M. Arbeiter, T. Fennel, and D. Bauer, Phys. Rev. Lett. **115**, 043001 (2015).
[49] V. Mosert and D. Bauer, Comput. Phys. Commun. **207**, 452 (2016).
[50] V. Tulsky and D. Bauer, Comput. Phys. Commun. **251**, 107098 (2020).
[51] S. Beaulieu, A. Comby, A. Clergerie, J. Caillat, D. Descamps, N. Dudovich, B. Fabre, R. Géneaux, F. Légaré, S. Petit, B. Pons, G. Porat, T. Ruchon, R. Taïeb, V. Blanchet, and Y. Mairesse, Science **358**, 1288 (2017).
[52] L. Nahon, G. A. Garcia, and I. Powis, J. Electron Spectrosc. Relat. Phenom. **204**, 322 (2015).
[53] M. Rechtsman, J. M. Zeuner, Y. Plotnik, Y. Lumer, D. Podolsky, F. Dreisow, S. Nolte, M. Segev, and A. Szameit, Nature (London) **496**, 196 (2013).
[54] R. Kahvedžić, D. Habibović, W. Becker, S. Gräfe, and D. B. Milošević, Ann. Phys. **535**, 2200616 (2023).